


Topological metal and a nonlinear Dirac point in the cubic Rashba model

Haijiao Ji , Ning Zhang, and Noah F. Q. Yuan*

Harbin Institute of Technology, Shenzhen 518055, People's Republic of China



(Received 29 February 2024; revised 9 April 2024; accepted 12 April 2024; published 30 April 2024)

We investigate the properties of the two-dimensional model with Rashba-type spin-orbit coupling cubic in electron momentum. In the normal phase, edge states emerge on open boundaries. In the superconducting phase, edge states could evolve into gapped fermionic edge states. Such edge states can be differentiated by the modulation of critical dc Josephson current of a tunnel junction under an out-of-plane magnetic field. Our results may apply to oxide interface superconductors.

DOI: [10.1103/PhysRevB.109.134520](https://doi.org/10.1103/PhysRevB.109.134520)

I. INTRODUCTION

The Rashba effect is one of the well-known manifestations of spin-orbit couplings (SOCs) in solids where inversion symmetry is broken by an electric field normal to the heterointerface [1,2]. Another well-known type of SOC due to the inversion symmetry breaking is the so-called Dresselhaus SOC [3]. In both cases, the SOC Hamiltonian is linear in electron momentum \mathbf{k} , and the electron spins exhibit one full winding in moving around the closed Fermi contour. Usually such \mathbf{k} -linear SOC is leading order effects in inversion symmetry breaking systems [4–6].

In certain systems the leading SOC will not be \mathbf{k} linear [7–11]. For example, in transition metal dichalcogenides (TMDs) [12–14] or the Kane-Mele model [15,16], due to the special point group symmetry, the leading order SOC near the Γ point is \mathbf{k} cubic, while the electron spin is pinned to the out-of-plane direction.

Other examples of nonlinear SOC can be found in interfaces such as (111) surface of GaAs quantum well [17,18], (001) surface of oxide SrTiO₃ (STO) [19–23], and Si-terminated (001) surface of the rare-earth antiferromagnet RRh₂Si₂ [24–26] (R denotes the rare-earth element such as Yb, Tb, etc.), where the \mathbf{k} -cubic Rashba SOC can well describe the dominant band structure, as verified by experiments [8,24]. In the GaAs quantum well, fine tuning is needed to cancel \mathbf{k} -linear Rashba and Dresselhaus effects [27]. When the dominant electrons are d (STO) or f orbitals (TbRh₂Si₂), the leading order SOC could become cubic [19,26].

Superconductivity has been found experimentally in some of the above systems with \mathbf{k} -cubic SOC, including bulk and two-dimensional (2D) TMDs [28–32], LaAlO₃/SrTiO₃ (LAO/STO) interfaces [33–35], and RRh₂Si₂ [36]. Correspondingly, unconventional superconductivity such as Ising superconductivity [37–39] and topological nodal superconductivity [12–14] has been found in 2D TMDs. It is therefore interesting to investigate the properties of superconductors

with \mathbf{k} -cubic SOC such as LAO/STO interfaces and RRh₂Si₂.

In this work, we focus on the abstract two-dimensional model equipped with the cubic Rashba SOC, and study both the normal and superconducting phases. In this cubic Rashba model, the SOC Hamiltonian is cubic in electron momentum \mathbf{k} , and the electron spins exhibit three full windings in moving around the closed Fermi contour, in contrast to the one full winding of the linear Rashba case. In the linear Rashba model, the so-called topological metal has been proposed to describe its normal phase [41–44], and the corresponding superconducting phase will also be affected to host finite-momentum superconductivity. In the cubic Rashba model, the notion of topological metal also applies to its normal phase, with edge states emerging on open edges, which could evolve into gapped fermionic edge states in the superconducting phase. Such exotic behaviors may have potential impacts on superconductors such as LAO/STO interfaces and RRh₂Si₂, for example on the Fraunhofer pattern of Josephson junctions as shown in Fig. 1.

II. TOPOLOGICAL METAL AND EDGE STATES

It is theoretically proposed and experimentally verified that the following cubic Rashba model could describe the low-energy band structure of interface superconductor LAO/STO [8]:

$$H_{\text{cR}}(\mathbf{k}) = \eta_0 k^2 + \eta_1 k^4 + \frac{1}{2} i \alpha (k_+^3 \sigma_- - k_-^3 \sigma_+), \quad (1)$$

with electron momentum $\mathbf{k} = (k_x, k_y)$, $k = |\mathbf{k}|$, $k_{\pm} = k_x \pm i k_y$, $\sigma_{\pm} = \sigma_x \pm i \sigma_y$, and Pauli matrices σ denoting spin. Here $\eta_{0,1}$ are coefficients for kinetic terms, and α is the cubic Rashba SOC coefficient.

The unitary symmetries of the cubic Rashba model form the point group D_{2d} with three generators: twofold in-plane rotation C_{2z} , twofold rotation $C_{2x'}$ along the diagonal direction $\mathbf{x}' \equiv (\hat{x} + \hat{y})/\sqrt{2}$, and in-plane mirror reflection $M_x : (k_x, k_y) \rightarrow (-k_x, k_y)$, $(\sigma_x, \sigma_y, \sigma_z) \rightarrow (\sigma_x, -\sigma_y, -\sigma_z)$. Though the point group is anisotropic, the energy bands of the cubic

*fyuanaa@connect.ust.hk

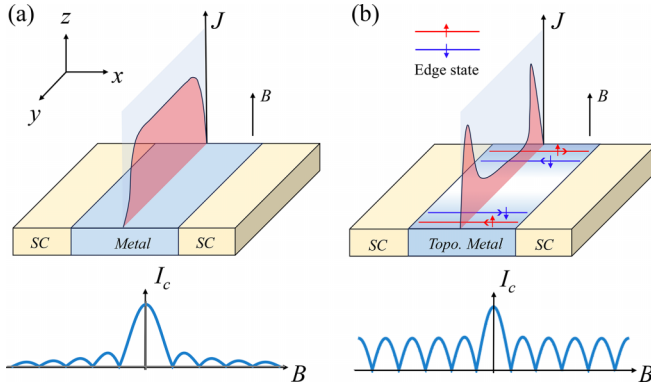


FIG. 1. Schematic picture of a Josephson junction under an out-of-plane magnetic field B in normal metal (a) or topological metal (b) with helical edge states (\uparrow, \downarrow denote spins). The spatial profile of supercurrent density $J(y)$ is shown correspondingly. The lower panels depict the critical current $I_c = \max | \int J dy dz |$ versus B in two cases, respectively.

Rashba model are isotropic

$$E_{\pm}(\mathbf{k}) = \eta_0 k^2 + \eta_1 k^4 \pm \alpha k^3, \quad (2)$$

and the two Fermi contours are hence circular and concentric. The inner (+) and outer (−) Fermi contours correspond to the upper (+) and lower (−) bands.

Due to the cubic Rashba SOC, electron spins have three full windings in moving around the Fermi contours as shown in Fig. 2(a), which can be characterized by the Berry phase π of both Fermi contours as enforced by the parity symmetries including time-reversal symmetry \mathcal{T} , mirror symmetries M_x, M_y , and combined symmetry $C_{2z}\mathcal{T}$. The metallic phase with quantized nonzero Berry phase π of the Fermi contours is known as the topological metal [40–44], which is consistent with quantum oscillation data of LAO/STO interfaces [22].

In the topological metal, there are odd numbers of Dirac points enclosed by the Fermi contours. However, the detailed properties of the Dirac point are not captured by the Berry phase, hence the properties of the topological metal is yet to be revealed.

For this purpose, we introduce the spin winding number to describe the topological property of the Dirac point

$$W = \frac{1}{2\pi} \text{Im} \oint_{\text{FS}} \frac{dS_x + i dS_y}{S_x + i S_y}, \quad (3)$$

where FS denotes the Fermi surface (or Fermi contour in 2D) and $\mathbf{S} = (S_x, S_y, S_z) = \langle \boldsymbol{\sigma} \rangle$ is the spin expectation value of the lower band E_- . The spin winding number of the cubic Dirac point in Eq. (1) can be worked out as $W = 3$. For linear Dirac point $H = \sum_{ij} k_i A_{ij} \sigma_j$, the spin winding number is $W = \text{sgn}(\det A)$. Calculations of the spin winding number can be found in the Appendix.

In the single-band metals, van Hove singularities in general exist and can be classified as ordinary and high-order ones [45,46]. In two-band metals, such as the cubic Rashba model in this work, band crossing points such as Dirac points generally exist, and could also be linear or nonlinear Dirac points (e.g., cubic Dirac point).

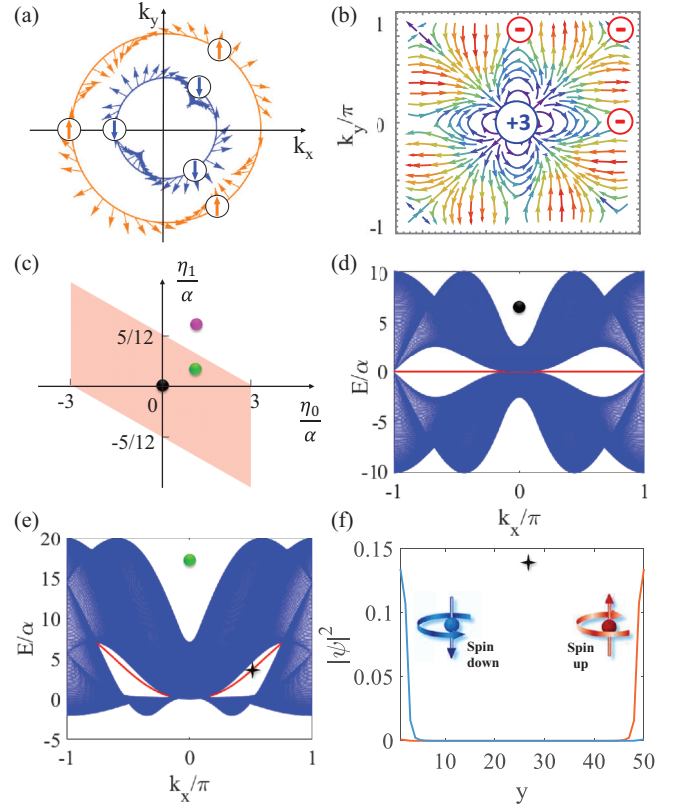


FIG. 2. (a) Spin texture of the Fermi contours of the cubic model Eq. (1). Electron spins have three full windings in moving around the Fermi contours. (b) The distribution of spin field (S_x, S_y) in the Brillouin zone, where the spin winding number $W = +3$ at the $\Gamma = (0, 0)$ point (colored blue), while $W = -1$ at $X = (\pi, 0), Y = (0, \pi)$ and $M = (\pi, \pi)$ points (colored red). The spin winding number W is defined in Eq. (3) and the spin field (S_x, S_y) is defined underneath. (c) Phase diagram of the cubic Rashba model Eq. (1), where edge states can be found explicitly in the pink region, for example the black (d) and green (e) dots, while edge states are mixed with bulk states in the white region such as the red dot [Fig. 5(a)]. (d) and (e) are corresponding energy spectra with open boundary conditions along the y direction with 200 lattice sites. (f) is the wavefunction of the edge states at momentum indicated by the black dagger in (e) with 50 lattice sites.

The cubic Rashba model Eq. (1) is defined near the Γ point. When this model is extended to the entire Brillouin zone (BZ), the Poincaré-Hopf index theorem dictates that the total spin winding number is zero

$$\sum_i W_i = 0. \quad (4)$$

The BZ compatible with point group D_{2d} would be that of a square lattice. Without loss of generality, we assume the lattice constant of the square lattice to be one. When the time-reversal-invariant points $X = (\pi, 0), Y = (0, \pi)$, and $M = (\pi, \pi)$ are linear Dirac points $|W_{X,Y,M}| = 1$ while Γ is cubic $W_{\Gamma} = 3$, the only choice of spin winding numbers is $W_{X,Y,M} = -1$ due to the Poincaré-Hopf index theorem, which is shown in the distribution of spin field (S_x, S_y) in the BZ in Fig. 2(b). There can be several ways to extend the continuous

cubic Rashba model Eq. (1) to the square BZ, leading to multiple tight-binding cubic Rashba models with the same nonlinear Dirac point described by Eq. (1) at the Γ point. Nevertheless, as we argued previously, the Poincaré-Hopf index theorem constrains the spin winding numbers at TRI points to be $W_{X,Y,M} = -1$. As a result, the topological properties associated with the spin winding number are not affected by details of the tight-binding model as long as the long-wavelength limit is the cubic Rashba model Eq. (1). Details of the tight-binding cubic Rashba model we used in this manuscript can be found in the Appendix.

The nontrivial spin winding number of the cubic Dirac point indicates the nontrivial bulk topology and hence topological edge states in the tight-binding model. In the phase diagram of Fig. 2(c), when the parameters $\eta_{0,1}/\alpha$ fall in the topological region (colored pink), the two energy bands are separated by local gaps as shown in Figs. 2(d) and 2(e). Under the open boundary condition of the x or y direction, edge states emerge whose dispersions are within local gaps [red lines in Figs. 2(d) and 2(e)], and whose wavefunctions are localized on two edges with opposite spin polarization along the z axis as shown in Fig. 2(f). Notice that the edge states are spin degenerate.

To figure out the origin of such edge states, we can consider the chiral limit $\eta_0 = \eta_1 = 0$ as shown in Fig. 2(d). In this chiral limit, the cubic model Eq. (1) has the chiral symmetry $\{H_{\text{CR}}, \sigma_z\} = 0$ and hence hosts zero energy modes on its open boundaries. Classified in the BDI class, nodal points of the bulk energy spectrum are characterized by the spin winding number W , and under open boundary condition, flat bands will emerge between projected nodal points with opposite spin winding numbers. In particular, when the y direction is open, the nodal points are projected to $k_x = 0$ with net spin winding number $W(k_x = 0) = +3 - 1 = +2$, and $k_x = \pm\pi$ with net spin winding number $W(k_x = \pm\pi) = -1 - 1 = -2$. Thus, a doubly degenerate flat band emerges connecting $k_x = 0$ and $k_x = \pi$, and another doubly degenerate flat band emerges connecting $k_x = 0$ and $k_x = -\pi \equiv \pi \pmod{2\pi}$. Furthermore, zero-energy edge states are eigenstates of chiral symmetry σ_z , and are hence spin polarized along the z axis. As shown in Fig. 2(f), we hence find spin-degenerate edge states.

Away from the chiral limit, one may treat $\eta_{0,1}$ as perturbations, under which the nodal points evolve into Dirac points connecting upper and lower bands, and the edge states become dispersive. As long as the local gaps are not closed, the corresponding edge states are protected by the bulk topology and separated from bulk states. As a result, we obtain the phase diagram of Fig. 2(c).

Topological metal under perturbations. We consider the following perturbations in the metallic phase

$$H_{\text{per}}(\mathbf{k}) = \frac{1}{2}i\lambda(k_+\sigma_+ - k_-\sigma_-) + \mathbf{B} \cdot \boldsymbol{\sigma}, \quad (5)$$

where λ is the linear Rashba coefficient and \mathbf{B} is the Zeeman field. These perturbations are allowed under point group D_{2d} , under which the number and positions of Dirac points of the band structure will change.

The spin-degenerate Dirac points can also be understood as the intersecting points of contours $S_x = 0$ (blue) and $S_y = 0$ (red), as plotted in Fig. 3. The cubic Dirac point as shown in Fig. 3(a) is the intersecting point of six contours, while linear

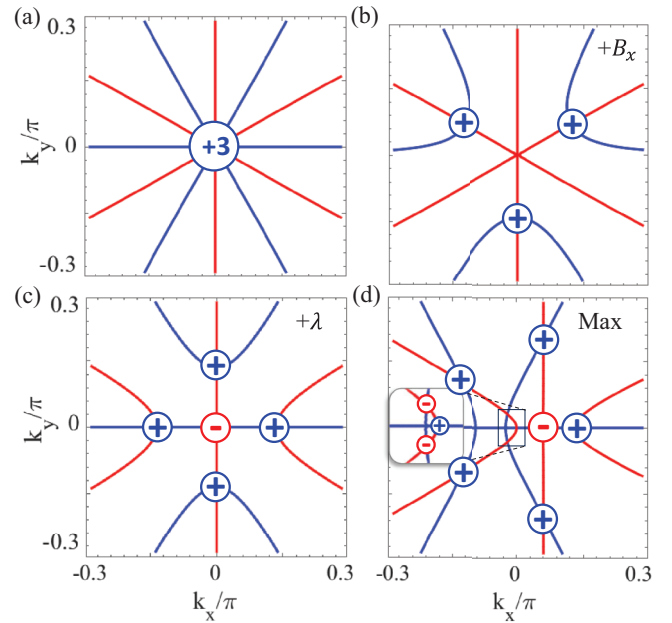


FIG. 3. Zero contours $S_x = 0$ (blue) and $S_y = 0$ (red) of the spin field (S_x, S_y) , and the intersecting points of blue and red lines are Dirac points with corresponding spin winding numbers. (a) One cubic Dirac point at zero field. (b) Three linear Dirac points under in-plane Zeeman field $B_x = 0.1\alpha$ along the x axis. (c) Five linear Dirac points under linear Rashba $\lambda = 0.1\alpha$. (d) Nine linear Dirac points under symmetry-breaking perturbations.

Dirac points as shown in Figs. 3(b)–3(d) are the intersecting points of two contours. To see this, notice that the cubic Dirac point has spin winding number $W = 3$, hence each spin polarization will appear three times along the Fermi contour enclosing cubic Dirac point. As a result, the polarized state $S_x = 0$ or $S_y = 0$ will appear three times, leading to three contours for $S_x = 0$ and three contours for $S_y = 0$ around the cubic Dirac point. In fact, when the Dirac point has spin winding number W , then there will be $|W|$ contours for $\mathbf{S} \cdot \hat{\mathbf{n}} = 0$ with any given in-plane direction $\hat{\mathbf{n}}$, and the Dirac point as a spin-degenerate point is the intersecting point of contours $\mathbf{S} \cdot \hat{\mathbf{n}} = 0$.

Under an in-plane Zeeman field, the single cubic Dirac point in Fig. 3(a) is split into three linear Dirac points as shown in Fig. 3(b), forming a threefold structure. Under the linear Rashba effect, the cubic Dirac point is split into five linear Dirac points as shown in Fig. 3(c), forming a fourfold structure. During the Dirac point splitting process, the total spin winding number in the neighborhood of the Γ point is conserved due to topology [45,46], as shown in Figs. 3(b) and (c). In fact, the two energy bands can be expressed in terms of the polar coordinates of the electron momentum $\mathbf{k} = k(\cos \theta, \sin \theta)$ as

$$E_{\pm}(\mathbf{k}) = \eta_0 k^2 + \eta_1 k^4 \pm D(k, \theta), \quad (6)$$

where the energy bands are threefold symmetric under an in-plane Zeeman field $\mathbf{B} = B(\cos \phi, \sin \phi)$, while fourfold

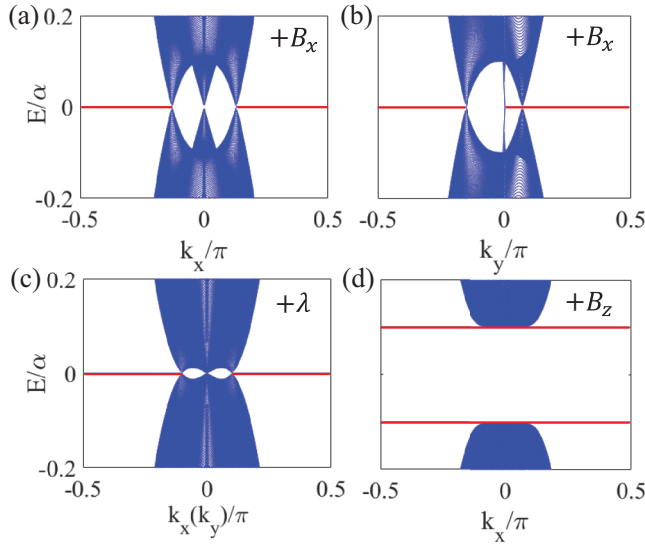


FIG. 4. Energy spectra near the Γ point in the chiral limit under external Zeeman fields (a), (b), (d) and linear Rashba effect (c), where edge states are in red color. Parameters are the same as Fig. 3, and $B_z = 0.1\alpha$ in (d).

symmetric under linear Rashba effect λ :

$$D(k, \theta) = \begin{cases} \sqrt{B^2 + \alpha^2 k^6 - 2B\alpha k^3 \sin(3\theta - \phi)} & \lambda = 0, \\ k\sqrt{\lambda^2 + \alpha^2 k^4 - 2\lambda\alpha k^2 \cos 4\theta} & B = 0. \end{cases} \quad (7)$$

With both in-plane Zeeman field and linear Rashba effect, the in-plane rotation symmetry of the energy bands is then lost. Derivation of Eq. (7) can be found in the Appendix. From Eq. (7), the Dirac point splitting under arbitrary in-plane Zeeman field direction ϕ can hence be deduced, and in Fig. 3(b) $\phi = 0$.

We introduce the multiplicity (also known as the Milnor number) μ of the Dirac point, which is defined as the maximal number of split Dirac points under perturbations [46]. Here perturbations are defined as the Hamiltonian terms with lower orders in momentum than that of the Dirac point. The cubic Dirac point can be split into at most five linear Dirac points under the symmetry-allowed perturbations in Eq. (5), hence the symmetry-constraint multiplicity of the cubic Dirac point is $\mu_{\text{sym}} = 5$. Without symmetry constraints, the cubic Dirac point can be split into at most $\mu = W^2 = 9$ linear Dirac points, as shown in Fig. 3(d) where the time-reversal symmetry \mathcal{T} is broken and the point group is reduced to $C_{1v} = \{1, M_y\}$.

We have discussed the effects of perturbations on the bulk spectrum, especially the Dirac points. Due to the bulk-edge correspondence, the edge states will also be affected. The general mechanism indicates that edge states will emerge between projected nodal points with opposite spin winding numbers. For simplicity we consider the chiral limit first. As shown in Fig. 4, edge states are found under open boundary conditions, which are flat bands in the chiral limit. Notice that under in-plane Zeeman field (a) and (b) and linear Rashba effect (c), the net spin winding numbers of the nodal points near the projected Γ point can become zero, ± 1 besides ± 2 .

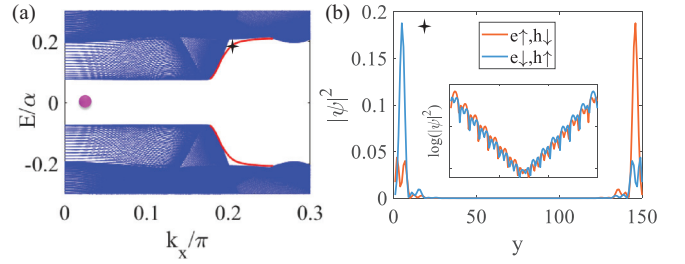


FIG. 5. (a) Superconducting spectrum under s -wave pairing $\Delta(k) = \Delta_0 + \Delta_1 k^2$. The red lines denote the gapped fermionic edge states. Parameters are $(\eta_0, \eta_1) = (1, \frac{1}{2})\alpha$ [red dot in Fig. 2(c)] and $(\Delta_0, \Delta_1) = (0, \frac{1}{4})\alpha$. (b) Edge state wavefunctions at the black dagger in (a), with electron/hole (e/h) and spin (\uparrow/\downarrow) components. Inset: Logarithm of edge state wavefunctions, showing the exponential localization of edge states.

Notice that under an out-of-plane field B_z (d), the spin-degenerate edge band will get split into two spin polarized bands, whose wavefunctions are similar to those shown in Fig. 2(f).

The introduction of kinetic terms $\eta_{0,1}$ will gradually close the local gaps, which disperse and eventually diminish edge states. In the following, we would like to show that even when kinetic terms close the local gaps and diminish edge states in the normal phase, fermionic edge states will get revealed under appropriate pairing potentials in the superconducting phase.

III. TOPOLOGICAL METAL UNDER PAIRINGS

We use Δ_{\pm} to denote the pairing gaps of the inner (+) and outer (−) Fermi contours, respectively, then as long as $\Delta_+ < \Delta_-$, fermionic edge states will be found. For example, one can consider the s -wave pairing with constant (Δ_0) and extended (Δ_1) parts $\Delta(k) = \Delta_0 + \Delta_1 k^2$, then $\Delta_{\pm} = \Delta(k_{F\pm})$ with Fermi momenta $k_{F\pm}$ of inner (+) and outer (−) Fermi contours, respectively. As shown in Fig. 5(a), when $\Delta_1 > 0$ and $\Delta_+ < \Delta_-$, the edge states (colored red) will emerge joining the inner (+) and outer (−) Fermi contours with pairing gaps Δ_+ and Δ_- , respectively, whose wavefunction is also localized on two open edges with opposite spin polarization along the z axis as shown in Fig. 5(b), where electron spin σ is equivalent to hole spin $-\sigma^*$. Importantly, when $\Delta_+ < \Delta_-$, fermionic edge states will be found in the superconducting phase, either the normal phase bulk and edge states are separated or mixed [Fig. 2(c) pink versus white regions, respectively], and whether the pairing is spin singlet, triplet, or mixed.

As depicted in Fig. 1(a), in a superconductor-normal metal-superconductor (SNS) Josephson junction, the supercurrent is in the bulk. In a superconductor-topological metal-superconductor (STS) Josephson junction, however, the supercurrent is both in the bulk and along the edge as depicted in Fig. 1(b).

Suppose the Josephson current density of a 1D channel is $J = J_c \sin \varphi$ with the Josephson phase difference φ and critical current density J_c . For edge states, there are two 1D channels along two opposite edges, respectively, as shown in Fig. 1(b).

Under an out-of-plane magnetic field with magnetic flux Φ , the edge Josephson current is

$$I_E(\varphi) = \frac{1}{2}J_c d l \sin\left(\varphi + \frac{\pi\Phi}{\Phi_0}\right) + \frac{1}{2}J_c d l \sin\left(\varphi - \frac{\pi\Phi}{\Phi_0}\right), \quad (8)$$

where $\frac{1}{2}l$ is the localization length of the edge states along the y axis, d is the sample thickness along the z axis, and $\Phi_0 = h/(2e)$ is the flux quantum. For bulk states, there is a continuum of 1D channels and the bulk current is

$$I_B(\varphi) = J_c d \int_{-L/2}^{L/2} dy \sin\left(\varphi + \frac{2\pi\Phi y}{\Phi_0 L}\right), \quad (9)$$

where L is the sample size along the y axis.

The critical current of a Josephson junction under an out-of-plane field including bulk and edge states is

$$I_c = \max_{\varphi} |I_B(\varphi) + I_E(\varphi)| \\ = \left| I_B \frac{\sin(\pi\Phi/\Phi_0)}{\pi\Phi/\Phi_0} + I_E \cos\left(\frac{\pi\Phi}{\Phi_0}\right) \right|, \quad (10)$$

where $I_B = J_c d L$ denote the Fraunhofer interference of the bulk states and $I_E = J_c d l$ denotes superconducting quantum interference of the edge states. For normal metal in Fig. 1(a), only bulk states carry supercurrent and I_c exhibits the Fraunhofer pattern. For topological metal in Fig. 1(b), edge states also carry supercurrent, and hence with increasing field, I_c can decay slower than that of the Fraunhofer pattern. In experiments, by appropriate transforms of the critical current $I_c(\Phi)$ [47], the supercurrent density distribution can be obtained, where the edge-localized supercurrent corresponds to edge states [30].

IV. CONCLUSION

In this work, we study the cubic Rashba model arising from LAO/STO interface superconductors. Topological edge states associated with the cubic Dirac point are found in the normal phase, which we call topological metal. Such edge states could evolve into various forms under perturbations such as linear Rashba SOC, Zeeman fields, and pairings, and can be revealed via analysis of the dc critical current of a Josephson junction under an out-of-plane magnetic field.

ACKNOWLEDGMENTS

We thank D.-H. Xu for bringing us the cubic Rashba model. We thank K.T. Law, B.Q. Lv, and Yuanfeng Xu for helpful discussions. This work is supported by the National Natural Science Foundation of China (Grant No. 12174021).

APPENDIX A: CALCULATION OF SPIN WINDING NUMBER

The spin vector component can be written in polar coordinates as follows: $S_x = S \cos \phi$, $S_y = S \sin \phi$, then according to

$$dS_x = \cos \phi dS - S \sin \phi d\phi, \\ dS_y = \sin \phi dS + S \cos \phi d\phi, \quad (A1)$$

Eq. (3) becomes

$$W = \frac{1}{2\pi} \oint_{\text{FS}} d\phi. \quad (A2)$$

The polar angle ϕ of the spin can be obtained from the spin vector field as plotted in Fig. 2(b). At the Γ point, using $k_x = k \cos \theta$, $k_y = k \sin \theta$, we find the eigenstates

$$H_{\text{cR}}(\mathbf{k})\psi_{\pm} = E_{\pm}(\mathbf{k})\psi_{\pm}, \quad \psi_{\pm} = \frac{1}{\sqrt{2}} \begin{pmatrix} 1 \\ \pm i e^{3i\theta} \end{pmatrix}. \quad (A3)$$

Then the spin vector is

$$\mathbf{S} = \psi_{-}^{\dagger} \boldsymbol{\sigma} \psi_{-} = \{\sin 3\theta, -\cos 3\theta, 0\} \quad (A4)$$

and, hence, for the nonlinear Dirac point at the Γ point,

$$\phi = 3\theta - \frac{\pi}{2}, \quad (A5)$$

which leads to $W = 3$.

For linear Dirac point $H = \sum_{ij} k_i A_{ij} \sigma_j$, one can work out eigenstates $H\psi_{\pm} = \pm E\psi_{\pm}$ and the spin

$$\mathbf{S} = \psi_{-}^{\dagger} \boldsymbol{\sigma} \psi_{-} = \mathbf{p}/|\mathbf{p}|, \quad \mathbf{p} = -A^T \mathbf{k}, \quad (A6)$$

where $A = \{A_{ij}\}$ is the 2×2 matrix formed by four coefficients A_{ij} . Alternatively, we can write

$$\mathbf{S} = \tilde{A} \frac{\mathbf{k}}{|\mathbf{k}|}, \quad \tilde{A} \equiv -\frac{A^T}{\sqrt{AA^T}}. \quad (A7)$$

Since \tilde{A} is now an orthogonal matrix, the spin winding number is $W = \text{sgn}(\det \tilde{A}) = \text{sgn}(\det A)$.

APPENDIX B: TIGHT-BINDING CUBIC RASHBA MODEL

The continuum cubic Rashba model reads

$$H_{\text{cR}}(\mathbf{k}) = \eta_0 k^2 + \eta_1 k^4 + \frac{1}{2} i \alpha (k_+^3 \sigma_- - k_-^3 \sigma_+), \quad (B1)$$

where

$$k^2 = k_x^2 + k_y^2, \quad k^4 = (k_x^2 + k_y^2)^2, \quad (B2)$$

$$k_+^3 = (k_x + i k_y)^3 = k_x^3 + 3i k_x^2 k_y - 3k_x k_y^2 - i k_y^3, \quad (B3)$$

$$k_-^3 = (k_x - i k_y)^3 = k_x^3 - 3i k_x^2 k_y - 3k_x k_y^2 + i k_y^3. \quad (B4)$$

Since the point group is D_{2d} , the tight-binding model should be built on a square lattice which contains linear combinations of $\cos k_{x(y)}$, $\sin k_{x(y)}$, and their products. The following substitution realizes power series of $k_{x(y)}$ in terms of $\cos k_{x(y)}$, $\sin k_{x(y)}$ and their products:

$$k_{x(y)} \rightarrow \sin k_{x(y)}, \\ k_{x(y)}^2 \rightarrow 2(1 - \cos k_{x(y)}), \\ k_{x(y)}^3 \rightarrow 2 \sin k_{x(y)}(1 - \cos k_{x(y)}). \quad (B5)$$

The tight-binding Hamiltonian becomes

$$H = -2\eta_0(\cos k_x + \cos k_y - 2) \\ + 4\eta_1(\cos k_x + \cos k_y - 2)^2 \\ + i\alpha(-4 \sin k_x + 6 \cos k_y \sin k_x - \sin 2k_x)\sigma_y \\ + i\alpha(-4 \sin k_y + 6 \cos k_x \sin k_y - \sin 2k_y)\sigma_x. \quad (B6)$$

Near the Γ point, according to the Taylor expansion, Eq. (B6) becomes

$$\begin{aligned} H &= 2\eta_0(k_x^2 + k_y^2) + 4\eta_1(k_x^2 + k_y^2)^2 \\ &\quad + \alpha(k_x^3 - 3k_x k_y^2)\sigma_y + \alpha(k_y^3 - 3k_y^2 k_x)\sigma_x \\ &= \eta_0 k^2 + \eta_1 k^4 + \frac{1}{2}i\alpha(k_+^3\sigma_- - k_-^3\sigma_+) + O(k^5). \end{aligned} \quad (\text{B7})$$

APPENDIX C: CALCULATION DETAIL OF EQ. (7)

The whole Hamiltonian of the cubic Rashba model with perturbations reads

$$\begin{aligned} H &= \eta_0 k^2 + \eta_1 k^4 + \frac{1}{2}i\alpha(k_+^3\sigma_- - k_-^3\sigma_+) \\ &\quad + \frac{1}{2}i\lambda(k_+\sigma_+ - k_-\sigma_-) + B_x\sigma_x + B_y\sigma_y, \end{aligned} \quad (\text{C1})$$

where $k^2 = k_x^2 + k_y^2$, $k_{\pm} = k_x \pm ik_y$, $\sigma_{\pm} = \sigma_x \pm i\sigma_y$. When writing the momentum and magnetic field in terms of polar coordinates $(k_x, k_y) = k(\cos\theta, \sin\theta)$, $(B_x, B_y) = B(\cos\phi, \sin\phi)$, the whole Hamiltonian becomes

$$H = \begin{pmatrix} \eta_0 k^2 + \eta_1 k^4 & \mathcal{D}^* \\ \mathcal{D} & \eta_0 k^2 + \eta_1 k^4 \end{pmatrix} \quad (\text{C2})$$

with $\mathcal{D} = i\alpha k^3 e^{3i\theta} + i\lambda k e^{-i\theta} + B e^{i\phi}$. The quantity $D(k, \theta)$ in Eq. (7) then reads $D = |\mathcal{D}|$, and hence,

$$\begin{aligned} D^2 &= \mathcal{D}\mathcal{D}^* = B^2 + \alpha^2 k^6 + \lambda^2 k^2 + 2\alpha\lambda k^4 \cos(4\theta) \\ &\quad - 2\alpha B k^3 \sin(3\theta - \phi) + 2B\lambda k \sin(\theta + \phi). \end{aligned}$$

APPENDIX D: SUPERCONDUCTING PHASE OF TOPOLOGICAL METAL

To investigate the superconducting properties of the cubic Rashba model, we consider the Bogoliubov-de Gennes

TABLE I. Possible pairings in the cubic Rashba model.

D_{2d}	ψ	\mathbf{d}
A_1	1 k^2 $k^4, \text{Re}k_+^4$	$k_y\hat{x} + k_x\hat{y}$ $k_x^2 k_y \hat{x} + k_y^2 k_x \hat{y}$ $k_y^3 \hat{x} + k_x^3 \hat{y}$
A_2	$\text{Im}k_+^4$	$k_x\hat{x} - k_y\hat{y}$ $k_x k_y^2 \hat{x} - k_y k_x^2 \hat{y}$ $k_x^3 \hat{x} - k_y^3 \hat{y}$
B_1	$\text{Im}k_+^2$	\mathbf{k} $k_x k_y^2 \hat{x} + k_y k_x^2 \hat{y}$ $k_y^3 \hat{x} + k_x^3 \hat{y}$
B_2	$\text{Re}k_+^2$	$\hat{z} \times \mathbf{k}$ $k_x^2 k_y \hat{x} - k_y^2 k_x \hat{y}$ $k_x^3 \hat{x} - k_y^3 \hat{y}$
E	0	$(\frac{k_x \hat{z}}{k_y \hat{z}}, (\frac{k_x k_y^2 \hat{z}}{k_x^2 k_y \hat{z}}), (\frac{k_x^3 \hat{z}}{k_y^3 \hat{z}}))$

(BdG) Hamiltonian as follows:

$$H_{\text{BdG}}(\mathbf{k}) = \begin{pmatrix} H_{\text{cR}}(\mathbf{k}) - \varepsilon_F & H_{\Delta}(\mathbf{k}) \\ H_{\Delta}^{\dagger}(\mathbf{k}) & -H_{\text{cR}}^*(-\mathbf{k}) + \varepsilon_F \end{pmatrix}, \quad (\text{D1})$$

where ε_F is the Fermi energy and the generic pairing is $H_{\Delta} = (\psi + \mathbf{d} \cdot \boldsymbol{\sigma})i\sigma_y$ with the spin-singlet $\psi(\mathbf{k})$ and spin-triplet $\mathbf{d}(\mathbf{k})$ pairings. Due to the Pauli exclusion principle, the spin singlet is even in momentum $\psi(-\mathbf{k}) = \psi(\mathbf{k})$ and spin triplet is odd $\mathbf{d}(-\mathbf{k}) = -\mathbf{d}(\mathbf{k})$. According to the symmetry group D_{2d} of the cubic Rashba model, the possible spin-singlet and spin-triplet pairings are calculated as shown in the Table I.

- [1] E. I. Rashba and V. I. Sheka, Symmetry of energy bands in crystals of wurtzite type II. Symmetry of bands with spin-orbit interaction included, *Fiz. Tverd. Tela: Collected Papers* **2**, 162 (1959).
- [2] Y. A. Bychkov and E. I. Rashba, Oscillatory effects and the magnetic susceptibility of carriers in inversion layers, *J. Phys. C* **17**, 6039 (1984).
- [3] G. Dresselhaus, Spin-orbit coupling effects in zinc blende structures, *Phys. Rev.* **100**, 580 (1955).
- [4] J. Nitta, T. Akazaki, H. Takayanagi and T. Enoki, Gate control of spin-orbit interaction in an inverted $\text{In}_{0.53}\text{Ga}_{0.47}\text{As}/\text{In}_{0.52}\text{Al}_{0.48}\text{As}$ heterostructure, *Phys. Rev. Lett.* **78**, 1335 (1997).
- [5] A. Manchon, H. C. Koo, J. Nitta, S. M. Frolov and R. A. Duine, New perspectives for Rashba spin-orbit coupling, *Nat. Mater.* **14**, 871 (2015).
- [6] G. Bihlmayer, O. Rader, and R. Winkler, Focus on the Rashba effect, *New J. Phys.* **17**, 050202 (2015).
- [7] R. Winkler, Rashba spin splitting in two-dimensional electron and hole systems, *Phys. Rev. B* **62**, 4245 (2000).
- [8] H. Nakamura, T. Koga, and T. Kimura, Experimental evidence of cubic Rashba effect in an inversion-symmetric oxide, *Phys. Rev. Lett.* **108**, 206601 (2012).
- [9] H. Liu, E. Marcellina, A. R. Hamilton, and D. Culcer, Strong spin-orbit contribution to the Hall coefficient of two-dimensional hole systems, *Phys. Rev. Lett.* **121**, 087701 (2018).
- [10] H. J. Zhao, H. Nakamura, R. Arras, C. Paillard, P. Chen, J. Gosteau, X. Li, Y. Yang, L. Bellaiche, Purely cubic spin splittings with persistent spin textures, *Phys. Rev. Lett.* **125**, 216405 (2020).
- [11] D. Y. Usachov, M. Güttler, S. Schulz, G. Poelchen, S. Seiro, K. Kliemt, K. Kummer, C. Krellner, C. Laubschat, E. V. Chulkov, and D. V. Vyalikh, Spin structure of spin-orbit split surface states in a magnetic material revealed by spin-integrated photoemission, *Phys. Rev. B* **101**, 245140 (2020).
- [12] W. Y. He, B. T. Zhou, J. J. He, N. F. Q. Yuan, T. Zhang, and K. T. Law, Magnetic field driven nodal topological superconductivity in monolayer transition metal dichalcogenides, *Commun. Phys.* **1**, 40 (2018).
- [13] A. K. Nayak, A. Steinbok, Y. Roet, J. Koo, G. Margalit, I. Feldman, A. Almoalem, A. Kanigel, G. A. Fiete, B. Yan, Y. Oreg, N. Avraham, and H. Beidenkopf, Evidence of topological boundary modes with topological nodal-point superconductivity, *Nat. Phys.* **17**, 1413 (2021).
- [14] A. Hamill, B. Heischmidt, E. Sohn, D. Shaffer, K.-T. Tsai, X. Zhang, X. Xi, A. Suslov, H. Berger, L. Forró, F. J. Burnell, J.

- Shan, K. F. Mak, R. M. Fernandes, K. Wang, and V. S. Pribiag, Two-fold symmetric superconductivity in few-layer NbSe₂, *Nat. Phys.* **17**, 949 (2021).
- [15] C. L. Kane, and E. J. Mele, Quantum spin Hall effect in graphene, *Phys. Rev. Lett.* **95**, 226801 (2005).
- [16] C. L. Kane, and E. J. Mele, Z₂ topological order and the quantum spin Hall effect, *Phys. Rev. Lett.* **95**, 146802 (2005).
- [17] T. Koga, J. Nitta, T. Akazaki, and H. Takayanagi, Rashba spin-orbit coupling probed by the weak antilocalization analysis in InAlAs/InGaAs/InAlAs quantum wells as a function of quantum well asymmetry, *Phys. Rev. Lett.* **89**, 046801 (2002).
- [18] G. M. Minkov, A. A. Sherstobitov, A. V. Germanenko, O. E. Rut, V. A. Larionova, and B. N. Zvonkov, Antilocalization and spin-orbit coupling in the hole gas in strained GaAs/In_xGa_{1-x}As/GaAs quantum well heterostructures, *Phys. Rev. B* **71**, 165312 (2005).
- [19] A. D. Caviglia, M. Gabay, S. Gariglio, N. Reyren, C. Cancellieri, and J. M. Triscone, Tunable Rashba spin-orbit interaction at oxide interfaces, *Phys. Rev. Lett.* **104**, 126803 (2010).
- [20] P. D. C. King, S. M. Walker, A. Tamai, A. de la Torre, T. Eknapakul, P. Buaphet, S.-K. Mo, W. Meevasana, M. S. Bahramy, and F. Baumberger, Quasiparticle dynamics and spin-orbital texture of the SrTiO₃ two-dimensional electron gas, *Nat. Commun.* **5**, 3414 (2014).
- [21] H. Liang, L. Cheng, L. Wei, Z. Luo, G. Yu, C. Zeng, Z. Zhang, Nonmonotonically tunable Rashba spin-orbit coupling by multiple-band filling control in SrTiO₃-based interfacial *d*-electron gases, *Phys. Rev. B* **92**, 075309 (2015).
- [22] M. J. Veit, R. Arras, B. J. Ramshaw, R. Pentcheva, and Y. Suzuki, Nonzero Berry phase in quantum oscillations from giant Rashba-type spin splitting in LaTiO₃/SrTiO₃ heterostructures, *Nat. Commun.* **9**, 1458 (2018).
- [23] W. Lin, L. Li, F. Doğan, C. Li, H. Rotella, X. Yu, B. Zhang, Y. Li, W. S. Lew, S. Wang, W. Prellier, S. J. Pennycook, J. Chen, Z. Zhong, A. Manchon, and Tom Wu, Interface-based tuning of Rashba spin-orbit interaction in asymmetric oxide heterostructures with *3d* electrons, *Nat. Commun.* **10**, 3052 (2019).
- [24] D. Y. Usachov, I. A. Nechaev, G. Poelchen, M. Guttler, E. E. Krasovskii, S. Schulz, A. Generalov, K. Kliemt, A. Kraiker, C. Krellner, K. Kummer, S. Danzenbacher, C. Laubschat, A. P. Weber, J. Sanchez-Barriga, E. V. Chulkov, A. F. Santander-Syro, T. Imai, K. Miyamoto, T. Okuda *et al.*, Cubic Rashba effect in the surface spin structure of rare-earth ternary materials, *Phys. Rev. Lett.* **124**, 237202 (2020).
- [25] I. A. Nechaev, and E. E. Krasovskii, Relativistic splitting of surface states at Si-terminated surfaces of the layered intermetallic compounds RT₂Si₂ (R=rare earth; T=Ir, Rh), *Phys. Rev. B* **98**, 245415 (2018).
- [26] S. Schulz, A. Y. Vyazovskaya, G. Poelchen, A. Generalov, M. Guttler, M. Mende, S. Danzenbacher, M. M. Otrokov, T. Balasubramanian, C. Polley, E. V. Chulkov, C. Laubschat, M. Peters, K. Kliemt, C. Krellner, D. Y. Usachov, D. V. Vyalikh, Classical and cubic Rashba effect in the presence of in-plane *4f* magnetism at the iridium silicide surface of the antiferromagnet GdIr₂Si₂, *Phys. Rev. B* **103**, 035123 (2021).
- [27] S. D. Ganichev, and L. E. Golub, Interplay of Rashba/Dresselhaus spin splittings probed by photogalvanic spectroscopy—A review, *Physica Status Solidi (b)* **251**, 1801 (2014).
- [28] X. Qian, J. Liu, L. Fu, and J. Li, Quantum spin Hall effect in two-dimensional transition metal dichalcogenides, *Science* **346**, 1344 (2014).
- [29] E. Sajadi, T. Palomaki, Z. Fei, W. Zhao, P. Bement, C. Olsen, S. Luescher, X. Xu, J. A. Folk, and D. H. Cobden, Gate-induced superconductivity in a monolayer topological insulator, *Science* **362**, 922 (2018).
- [30] W. Wang, S. Kim, M. Liu, F. A. Cevallos, R. J. Cava, and N. P. Ong, Evidence for an edge supercurrent in the Weyl superconductor MoTe₂, *Science* **368**, 534 (2020).
- [31] S. Kezilebieke, M. N. Huda, V. Vaño, M. Aapro, S. C. Ganguli, O. J. Silveira, S. Głodzik, A. S. Foster, T. Ojanen, and P. Liljeroth, Topological superconductivity in a van der Waals heterostructure, *Nature (London)* **588**, 424 (2020).
- [32] E. Zhang, Y.-M. Xie, Y. Fang, J. Zhang, X. Xu, Y.-C. Zou, P. Leng, X.-J. Gao, Y. Zhang, L. Ai, Y. Zhang, Z. Jia, S. Liu, J. Yan, W. Zhao, S. J. Haigh, X. Kou, J. Yang, F. Huang, K. T. Law, Spin-orbit-parity coupled superconductivity in atomically thin 2M-WS₂, *Nat. Phys.* **19**, 106 (2023).
- [33] L. Li, C. Richter, J. Mannhart, and R. C. Ashoori, Coexistence of magnetic order and two-dimensional superconductivity at LaAlO₃/SrTiO₃ interfaces, *Nat. Phys.* **7**, 762 (2011).
- [34] J. A. Bert *et al.*, Direct imaging of the coexistence of ferromagnetism and superconductivity at the LaAlO₃/SrTiO₃ interface, *Nat. Phys.* **7**, 767 (2011).
- [35] Y. L. Han *et al.*, Two-dimensional superconductivity at (110) LaAlO₃/SrTiO₃ interfaces, *Appl. Phys. Lett.* **105**, 192603 (2014).
- [36] E. Schuberth, M. Tipmann, L. Steinke, S. Lausberg, A. Steppke, M. Brando, C. Krellner, C. Geibel, R. Yu, Q. Si, and F. Steglich, Emergence of superconductivity in the canonical heavy-electron metal YbRh₂Si₂, *Science* **351**, 485 (2016).
- [37] J. M. Lu, O. Zheliuk, I. Leermakers, N. F. Q. Yuan, U. Zeitler, K. T. Law, and J. Ye, Evidence for two-dimensional Ising superconductivity in gated MoS₂, *Science* **350**, 1353 (2015).
- [38] B. T. Zhou, N. F. Q. Yuan, H. L. Jiang, and K. T. Law, Ising superconductivity and Majorana fermions in transition-metal dichalcogenides, *Phys. Rev. B* **93**, 180501(R) (2016).
- [39] S. C. de la Barrera, M. R. Sinko, D. P. Gopalan, N. Sivasdas, K. L. Seyler, K. Watanabe, T. Taniguchi, A. W. Tsien, X. Xu, D. Xiao, and B. M. Hunt, Tuning Ising superconductivity with layer and spin-orbit coupling in two-dimensional transition-metal dichalcogenides, *Nat. Commun.* **9**, 1427 (2018).
- [40] X. Ying, and A. Kamenev, Symmetry-protected topological metals, *Phys. Rev. Lett.* **121**, 086810 (2018).
- [41] A. Alexandradinata, C. Wang, W. Duan, L. Glazman, Revealing the topology of Fermi-surface wave functions from magnetic quantum oscillations, *Phys. Rev. X* **8**, 011027 (2018).
- [42] C. Wang, W. Duan, L. Glazman, A. Alexandradinata, Hidden quasi-symmetries stabilize non-trivial quantum oscillations in CoSi, *Phys. Rev. B* **100**, 014442 (2019).
- [43] S. Sun, Z. Song, H. Weng, X. Dai, Topological metals induced by the Zeeman effect, *Phys. Rev. B* **101**, 125118 (2020).
- [44] N. F. Q. Yuan, and L. Fu, Topological metals and finite-momentum superconductors, *Proc. Natl. Acad. Sci. USA* **118**, e2019063118 (2021).
- [45] N. F. Q. Yuan, H. Isobe, and L. Fu, Magic of high-order van Hove singularity, *Nat. Commun.* **10**, 5769 (2019).

- [46] N. F. Q. Yuan, and L. Fu, Classification of critical points in energy bands based on topology, scaling, and symmetry, *Phys. Rev. B* **101**, 125120 (2020).
- [47] R. C. Dynes and T. A. Fulton, Supercurrent density distribution in Josephson junctions, *Phys. Rev. B* **3**, 3015 (1971).